Development of a 50th Percentile Female Femur Model

Development of a 50th Percentile Female Femur Model

A. Schubert, N. Erlinger, C. Leo, J. Iraeus, J. John, C. Klug

Abstract This study illustrates the development of a generic femur model representative of a 50th percentile female in terms of geometry, material data, and injury risk curve.

A female femur model consisting of 14,520 hexahedral elements was developed, calibrated, and validated. The outer shape and cortical thickness of the femur shaft were adjusted to meet a regression model reported in literature for an average 50 year old female. For the proximal femur, five computed tomography scans were morphed to the target geometry and the mean thickness of the cortical bone was calculated. Material properties for the cortical bone were calculated from experimental data for both tension and compression loading. To validate the proximal femur mode and calibrate an injury risk curve, 15 dynamic drop-tower tests were reproduced. For the validation of the femur shaft, 16 bending tests were simulated. The characteristics of the experimental curves were generally well captured for experiments with normal bone density. Maximum principal strains and 99th percentile strains of the cortical bone at the time of fracture were used to develop risk curves for fractures of the proximal femur and the femur shaft, which were identified as the most relevant femoral injuries in an accident analysis. The model as well as the post-processing scripts are openly available and can be applied or further enhanced by other researchers.

Keywords Female, femur, human body model, injury risk, sex-specific, VIVA+.

I. INTRODUCTION

Vulnerable Road Users (VRUs) are at disproportionately high risk of injury and death, with pedestrians, cyclists and drivers of motorised two- and three-wheeled vehicles, together accounting for 54 % of all global traffic fatalities [1]. To mitigate some of these severe injuries, car manufacturers develop and implement dedicated VRU safety measures. In the development as well as the assessment of these safety systems, experimental testing with isolated impactors is still extensively used although several limitations are inherent. The last decade has seen an increase in the use of human body models (HBMs) for such use cases, since these models often offer better biofidelity and allow the consideration of additional outputs [2]–[4]. Previous studies have shown that injuries to the lower extremities are highly relevant for VRUs when involved in passenger-car accidents [5]–[9]. It has been observed that the risk of female pedestrians and cyclists sustaining femur fractures is higher, based on the analysis of two different accident databases [5].

One of the benefits of HBMs is the possibility to replicate human diversity, which means that characteristics such as height, weight, body mass index (BMI), age and sex, can be considered through morphing [10]. However, the vast majority of currently available HBMs is based on computed tomography (CT) scans of individuals with the appropriate target anthropometry, generally a 50th percentile male [11]. While these models have been morphed into other anthropometries to cover a greater range of occupant heights and weights, models representing average females are still scarce. Efforts have been made by [12-13] to develop average female HBMs, the first one being a modified version of an existing model (Total Human Model for Safety (THUMS) 5th percentile female) while the latter is a new open-source model developed based on a 31-year-old female subject close to the 50th percentile anthropometry (original VIVA model). Both studies focused on the assessment of whiplash associated disorders and therefore turned their attention specifically to the modelling of the cervical spine and validation by means of rear impact load cases. The extremity bones of the original VIVA model were modelled as rigid bodies, as the deformation of these parts is not associated with a notable impact to the simulation of rear impacts (whiplash).

Within the Horizon 2020 project, VIRTUAL [12], the original VIVA model has been significantly updated and turned into a family of models. The new family of models is called the VIVA+ models [15] and will be used in new load cases (high severity occupant impacts, pedestrian and cyclist impacts). Both, the VIVA+ HBM model and the

Corina Klug is Assistant Professor (email: corina.klug@tugraz.at, phone: +43 316 873 30329), Alexander Schubert is a Master Student, Nico Erlinger a Research Assistant, Christoph Leo a PhD student at the Vehicle Safety Institute at Graz University of Technology, Austria. Johan Iraeus is Researcher and Jobin John is Postdoc at Chalmers University of Technology, Gothenburg, Sweden.

validation setups will be publically available on the VIRTUAL project OpenVT platform (https://virtual.openvt.eu).

The aim of this study was to develop and validate a generic femur model for the VIVA+ 50th percentile female (VIVA+ 50F) model, applicable for virtual testing procedures with a specific focus on VRUs. To be aligned with the rest of the VIVA+ 50F model, the aim was to make the generic femur representative of an average woman, with a stature of 162 cm and a BMI of 24 kg /m² (based on [13]). The target age was set to 50 years, as this corresponds with the average age of the European adult population [14]. To make the model applicable for virtual testing procedures, it must be accompanied by assessment criteria and a related injury risk curve. The development of the generic 50F femur model and the associated injury risk curves are described within this paper.

II. METHODS

A. Accident Analysis of Femur fractures

Analysis of datasets for Austria, the Netherlands and Sweden, [5] has concluded that females have significantly higher odds of sustaining fractures of the lower extremities. Therefore, detailed data was collected including full abbreviated injury scale (AIS) codes from three national databases (Central Database for In-Depth Accident (CEDATU, Austria), Swedish Traffic Accident Data Acquisition (STRADA, Sweden) and Bestand geRegistreerde Ongevallen (BRON, the Netherlands)). For this study, accident data has been reanalysed focusing on types of femur fractures sustained in pedestrian and cyclist accidents.

B. Geometry Update – Cortical Bone Thickness

The outer geometry of the generic femur model and the cortical cross-section of the femur shaft was defined in a previous step based on findings by [15]. Therefore, the cortical thickness of the shaft was adjusted at five locations to meet the reported regression model for the targeted HBM age, height and BMI. However, information about cortical thickness in the proximal femur region of the bone was limited as the cross-section area was reported only for one location. In order to obtain detailed cortical thickness distribution, finite element models based on CT scans (Siemens SOMATOM Definition, 120 kVp, 100–400 mAs, 512x512 matrix, 1.0 pitch, 300–400 mm FOV, 1.0-mm slice thickness, up-sampled with Lanczos filter kernel) of five female femoral heads (average age=24.6 years, avg. height=168.2 cm, avg. weight=61.5 kg) provided by [16] were used. It was decided to use the averaged data from all available specimens (average) rather than data from the only individual volunteer close to the target age of 50 years, as this would probably result in a more extensive limitation. The five surface models each contained the cortical thickness information. The method shown in Fig. 1 was applied to average and transfer this information to the generic average femur model. All subjects and the target geometry were landmarked manually with a slightly modified definition of [17], as shown in Appendix A (Fig. A-1). The individual specimen meshes were subsequently morphed to fit the target geometry using a custom Matlab script. Making use of the internal ANSA (Version 20.1.0, BETA CAE Systems) function *Results Mapper*, each specimen's thickness information was projected to the nodal thickness definition of the shell elements representing the outer surface of the VIVA+ femur mesh, resulting in five identical meshes with varying thickness information. For each node, the average thickness from the five meshes was calculated, giving the final thickness distribution. Using the ANSA function *Volumize*, the shell elements were converted to solids with the appropriate dimensions. Finally, the hexa-boxes of the trabecular and cortical bone were remodelled to match the new inner geometry.

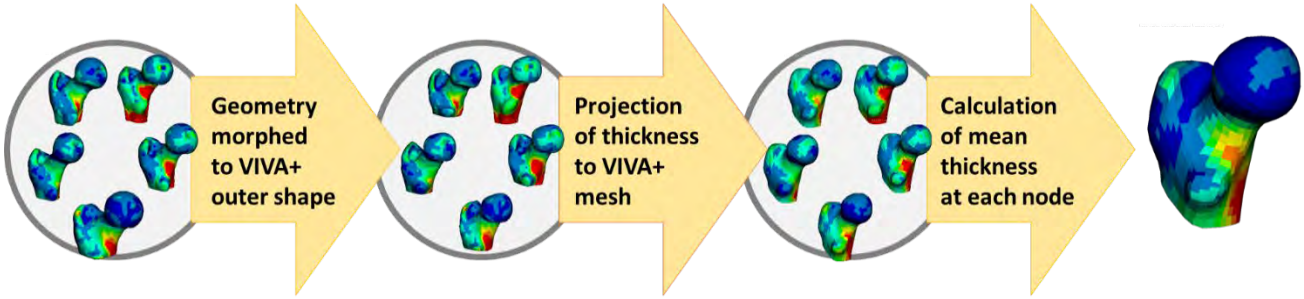

Fig. 1. Mean cortical thickness calculation process.

C. Material Models and Material Properties

1) Cortical Bone

The cortical bone is generally characterised as a transversely isotropic material with an asymmetric behaviour in tension and compression. Therefore, the LS-DYNA *MAT124, an elastic-plastic material model with the option of including individual strain-stress curves for tension and compression, was used. Raw data from experimental uniaxial tests with dumbbell samples of the mid femur shaft originally published by [18] was shared by the authors of that study for this specific purpose. The dataset contained data from 17 tensile, 17 compression and 13 torsion tests of female femur specimens. Since no anisotropic material model was developed, only the tensile and compression data was used. The mean age of the 17 female donors of the tension and compression loading tests was 76 years (SD 12). The supplied dataset consisted of signals for stroke, force, strain (directly captured in the axial channel), angle, torque, and radial extension/necking. Since the data also covered three preloading circles, the data was initially trimmed. To achieve this reliably, the timestamp of the last zero-crossing of the force signal for compression and tension, before loading cycle until initiating fracture, was identified automatically, checked manually, and all signals were cut off at this point. In order to minimise the signal noise, a Savitzky-Golay filter (window size 72, polynomial order = 1) and subsequent smoothing (window size 32) was applied. The actuator displacement was offset using the *first-value-offset* function and signals were cut off at maximum force. Subsequently, one sample subjected to compression loading and two specimens subjected to tension loading were excluded, since the remaining signals recorded in these experiments were much shorter (outside of mean+/-1.8 SD) than the mean strain of the other samples.

As fracture occurred at different strains for each bone specimen, the method described in [4] was used to calculate the mean curve. With this method, multiple signals can be used in their original sample rate and length without scaling. Ordinary arithmetic mean values were calculated for the duration of the shortest signal, however, subsequently to avoid *jumps* in the averaged curve the algorithm used a different approach: Instead of calculating the mean value, the mean slope at a given point was used to add a segment to the mean curve. The mean slope dictates the direction of the mean after the point where the first curve has ended. The force F and strain ε_{eng} signals were averaged independently to facilitate post-processing and can be seen in Appendix C (Fig. C-1).

Engineering stress-strain curves were calculated using the calculated averaged curves of the supplied material testing data. Subsequently, true stress-strain curves were calculated by applying the approach presented in [19]. A Python script was used to identify the linear range of the stress-strain curves and calculate the Young's moduli for compression and tension. The yield points were identified using a strain offset criterion of 0.05%.

The calibrated elastic-plastic material model was verified using a single element setup under compression and tension loading conditions. All simulations for this study were run in LS-DYNA MPP Version R 9.3.0 with single precision.

Based on findings by [20]–[22] and the implementation by [23]–[24], the strain-stress curves and the Young's moduli were scaled down for use in the greater trochanter area (factor 0.76 [20]), femur head and the femur neck (factor 0.44 [23]–[24]).

2) Trabecular Bone

The trabecular bone was modelled using a crushable foam material (Fu Chang foam, *MAT83) since it corresponds to the behaviour of bone tissue [25]. Although the density of trabecular bone varies greatly in the proximal femur, a pooled value of 0.27 g/cm^3 provided by [26] for the trabecular bone, was used. To gather the stress-strain curves for the material model, formulas from [27-28] were implemented in a Python script, and the corresponding stress-strain curves for six strain rates from 1E^{-6} to 10000 ms^{-1} were calculated for tension and compression. The Young's modulus E_{trab} was calculated using Equation 1 as proposed by [26], who determined the relationship based on experimental testing of 27 femoral neck specimens.

$$E_{trab} = 6850 * \rho^{1.49} \quad (1)$$

Next, the strain rate scaling factor SRS was calculated following the routine proposed by [27] (Equation 2), which has also been used by [28] and [29].

$$SRS = (\dot{\varepsilon}/0.005)^{0.06} \quad (2)$$

Finally, yield stress and proportional limit stress were calculated using the formulas given in [29], who refer to [27]–[28], [30]–[31]. The formulas are based on experimental testing and are summarised in Table I.

TABLE I
SUMMARY OF THE USED FORMULAS FOR THE CALCULATION OF STRESS AND STRAIN FOR *MAT83

	stress $\boldsymbol{\sigma}$	strain $\boldsymbol{\varepsilon}$
ultimate σ_u / ε_u	$49.5 * \rho_{app}^2 * SRS$	0.02
yield σ_y / ε_y	$\sigma_{ult}/1.1$	$\sigma_y/E + 0.02$
proportionality limit σ_p / ε_p	$\sigma_y * 0.8$	σ_p/E

For the tensional values, the ultimate stress and ultimate strain were multiplied by a compression/tension ratio of 0.7, based on the findings by [32]. Yield and proportionality limits were also calculated using the formulas stated in Table I.

The trabecular bone material was defined with different post-yield behaviours for tension and compression. For tension, the relationship proposed by [29] was used, which describes the behaviour as exponential decay as a function of strain (Equation 3).

$$\sigma_d = \sigma_u * (0.9 * e^{-25*\varepsilon_t} + 0.1) \quad (3)$$

For compression loading conditions, the description from [30] was followed: After yielding, the trabecular bone exhibited a plateau (collapse of the pores) until the crushed trabeculae came into contact again, which led to rapid hardening of the material. To avoid numerical issues, the curves were extended subsequent to the calculated maximum stress following the parabola defined for the hardening process. As was done for the cortical bone material, the material properties of the Fu Chang foam were also verified using a single element setup for compression and tension loading.

D. Validation

Two different experiments were replicated to address two different injury types addressed in the accident analysis – femur shaft fractures and proximal femur fractures. Experimental and simulated curves were compared objectively according to ISO 18571 [45] up to the time of fracture in the experiments.

1) Proximal Femur - Sideways Fall

The validation setup for the proximal femur corresponded to the widely described sideways fall (SWF) scenario of 10° abduction and 15° internal rotation. This configuration was first mentioned by [33] and later modified by [34]–[35]. Despite the popularity of this setup, see [30], [36]–[41], no detailed description of all geometric boundary conditions could be found. The simulation setup was modelled based on simulations of the setup by [42] which was also used and described in [43]–[44].

The distal end of the femur was potted in an aluminium cylinder using Polymethyl methacrylate (PMMA) with a potting length of 182 mm [28]. The potting was modelled using two parallel beam-elements with estimated inner and outer diameters of the PMMA-potting and the aluminium cylinder. A constrained nodal rigid body constraint (CNRB) was used to connect the beams at the starting point of the potting as well as the end, where the revolute joint was located, to the cortical nodes around the femur shaft. Additionally, the degrees of freedom of the CNRB at the femur end was restricted except for a rotation around the horizontal axis to mimic the boundary conditions described in [28].

PMMA-pads with a mass of about 21 g each for the head and greater trochanter (GT) were modelled to match the bone surface and meshed with similar parameters as the femur mesh was created. The elastic material property for PMMA was set to the same value as used by [28]. A rigid plate was modelled on top of the GT-pad, which was used for the application of the test specific displacement curves. A surface to surface contact was included between the bone and the PMMA-pads, and a generic friction coefficient (static, with a decay coefficient of zero) of 0.01 was applied in the contacts between the null shell covering the cortical bone and the PMMA-pads, to mimic the frictionless contact definition used by [28]. The setup of the SWF simulation is shown in Fig. 2.

All 14 tests by [28], featuring female specimens with a mean age of 76 years (SD 11), were reproduced. A single test of a male specimen was excluded. All tested specimens were derived from individual donors. The validation of the femur model under SWF loading conditions was carried out by applying the digitised (WebPlotDigitizer v4.4, https://automeris.io/WebPlotDigitizer) displacements from [42] to the top rigid plate of the simulation

model. The displacement data was originally obtained from target tracking using high-speed video data of the contact interface between the GT and the top PMMA-potting. The displacement curves of the rigid plate are shown in Appendix C (Fig. C-2). In contradiction to the simulations of [28], in order to limit localised force concentrations in the contact area of the GT, the top PMMA-pad was not modelled using a rigid material. The elastic compression of the upper pad (less than 0.01 mm) was found to be negligible for the simulation outcome.

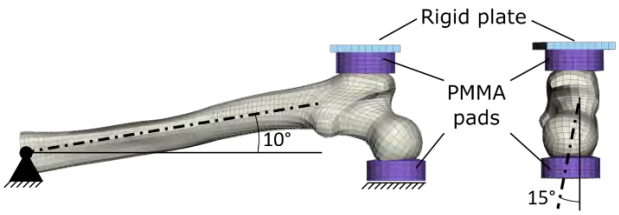

Fig. 2. Sideways fall simulation (SFW) setup for the proximal femur loading for the replication of tests conducted by [28].

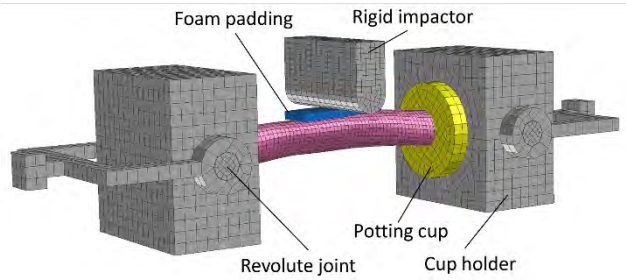

Fig. 3. Simulation of the setup for femur shaft loading for the replication of tests conducted by [45].

2) Femur Shaft - combined Axial Compression and Three-point Bending and Pure Three Point-bending

The femur model was also tested in the load case proposed and documented by [45]. In this setup, the bones were subjected to combined axial compression and bending in sagittal plane as well as pure three-point bending in sagittal plane loadings. The force magnitude in the axial direction was controlled using honeycomb inserts with different crush strengths resulting in loads of 4, 8, 12 and 16 kN (whereas 16 kN was only applied to male specimens). The impactor load was applied in a dynamic manner with a displacement rate of 1.5 m/s. Single tests were run with a quasi-static impactor speed of 1 mm/s. A total of 20 female specimens were tested in the study, out of which 11 with combined (one quasi-static), five with pure bending loading conditions and four under sole axial compression. The axial compression tests with female specimen were not replicated within the scope of the current study, as they are of relevance for vehicle occupants. Of these selected specimens 10 were tested under anterior-posterior (AP) loading conditions and six under posterior-anterior loading conditions (PA). For the simulations, the distal and proximal ends of the femur were cut (similar to the experimental protocol described in [45]) and the ends as were embedded in pottings, as shown in Fig. 3. The potting material (urethane cast), as well as the cup holders (aluminium) were modelled using a rigid material, however inertia was taken into account using realistic material densities. Coupling between the femur nodes inside the potting and the potting nodes was realised by a constrained extra node definition. Impactor displacement curves and axial force curves (for combined loading), as measured during the respective test, were included for each simulation. Raw data from the experiments was downloaded from National Highway Traffic Safety Administration (NHTSA) Biomechanics Test Database (www.nhtsa.gov/research-data/databases-and-software). For the prescribed impactor displacement, the displacement-time histories reported in the publication [45] were digitised using WebPlotDigitizer v4.4, to correct for vertical potting displacements, caused by elastic deformation of the rods connecting the cup holders to the load cells.

Furthermore, the 6.2 mm thick foam padding between the impactor and the femur, which was used in order to minimise localised stress peaks, was modelled using MAT_Low_Density_Foam including the material characterisation reported in the publication. The average age of the nine individual female donors (six for combined tests and three for pure bending tests) used for the replicated tests, was 53 years (SD 8). To bring simulation time to an acceptable level (fracture occurred at approx. 65 s after the test start), the quasi-static test (1.29) was run with an increased impactor speed of 100 mm/s instead of the original speed of 1 mm/s. This deviation was deemed acceptable, as only negligible influence on the simulation outcome was observed, when reducing the impactor speed further towards the tested speed. In addition, a time shift was applied for both the test data and the simulation in the shown plot.

E. Injury risk curve

The model-specific injury risk curve (IRC) for the proximal femur and the femur shaft were created based on simulated maximum principle strain (MPS) values, evaluated from the developed female femur model. The MPS values of the cortical bone at the time of the fracture were extracted using the Dynasaur [46] function

stress_strain_time_history with the settings mean integration point, *overall* for tension and compression and linear interpolation. Previous studies have shown that basing the calculations on the maximum value of a single element is highly sensitive to possible numerical issues, therefore, in addition to the MPS, the 99th percentile PS (PS99) MPS were considered [47].

The definition of fracture was used in accordance with the definition used by the original authors in [28]: The time of the peak force was considered as time of fracture occurring. Two bones (H1373R and H13380R) did not show total collapse during the experiments, which prevented a force drop after the initial peak, for these bones the first force peak was used as the reference for fracture.

The authors of the femur shaft experimental data showed that the occurrence of fracture could be determined using two methods: The drop of the force measured at the impactor and the point of drastic strain reduction matched exactly and identified the point of fracture in the femoral shaft (in addition, with the exception of the few experiments in which a delay of a few milliseconds was measured, the signal of the load cells below proximal and distal pottings also suggested the same fracture time) [45]. The time of peak force was identified for each specimen from the experimental raw data of the impactor load cell.

The dataset for the validation of the femur shaft consisted of 16 tests, whereas two tests were excluded from the injury risk curve calculation. Test 1.32 and 1.33 (both from the same 52 year old donor) had the lowest fracture force of 1.6 kN and 2.1 kN, respectively, leading also to remarkably small strain values compared to the other simulations. PS99 values of 0.0057 (1.32) and 0.0050 (1.33) were evaluated at time of fracture. In order to avoid the bias that would be caused by these low strain values, it was decided to exclude both simulations from the IRC calculation. Hence, for the femur shaft, the 14 validation simulations of the experiments on female specimen by [45] were used for calculating the risk curve .

For the proximal femur, at the time of experimental peak force, displacements of the GT in the range of 0.8 (H1167L) to 4.0 mm (H1381R) with a mean value of 2 mm (SD 0.9) were measured. Two experiments were out of a range, defined by the mean +/- standard deviation (SD), with a notable higher displacement at time of peak force: H1375L (4.0 mm), H1376L (3.7 mm). Simulation results also suggested noticeable increased strain values (PS99: 0.0652, 0.0576) compared to the other simulations. In addition, a notable increased strain value of PS99 was observed for H1381R (third largest displacement of 2.9 mm): 0.368 was evaluated. It was decided to consider these three tests and the corresponding simulation results as outliers, and to exclude them from the IRC development to avoid biasing.

A survival analysis was performed in R (Version 4.0.3) and the package *flexsurvreg* was used to fit the parametric models. Parameters for the Weibull functions were estimated with maximum likelihood estimation.

III. RESULTS

A. Accident Analysis of Femur Fractures

The distribution of the femur fractures for pedestrians and cyclists, for the different datasets from Austria, the Netherlands and Sweden, can be seen in Table II. It can be seen that the majority of femur fractures included in the datasets for the Netherlands (pedestrians: 66%, cyclists: 66%) and Sweden (pedestrians: 50%, cyclists: 80%) are related to proximal femur fractures, whereas the majority of femur fractures in the Austrian data was not further specified (pedestrians: 90%, cyclists 75%). As the second most common fracture type, fracture of the femur shaft was identified with a share of 66% (pedestrians and cyclists) for the Netherlands and 50% (pedestrians) and 80% (cyclists) for Sweden, respectively. Female and male accident data, shown in Table II, has been pooled as a similar femur fracture trend was observed for both.

TABLE II

DISTRIBUTION OF FEMUR FRACTURES IN THE DIFFERENT DATABASES BASED ON DATA FROM [5] (NFS = NOT FURTHER SPECIFIED)

	Austria		Netherlands		Sweden	
	Pedestrian *n=10*	Cyclist *n=4*	Pedestrian *n=342*	Cyclist *n=863*	Pedestrian *n=34*	Cyclist *n=20*
Proximal femur fracture	0%	0%	**66%**	**66%**	**50%**	**80%**
Femur shaft fracture	10%	0%	15%	15%	32%	20%
Distal femur fracture	0%	25%	10%	10%	15%	0%
NFS femur fracture	**90%**	**75%**	9%	9%	3%	0%

B. Cortical Thickness

The cortical thickness distribution of the femur head, derived from the average of five CT scans, is shown in Fig. 4. The values show strong local differences ranging from approx. 1 mm in the head and the greater trochanter region to approx. 5 mm in the region dorsal to the lesser trochanter. The femur head was divided into five regions, for which averaged thickness values have been summarised in Table III.

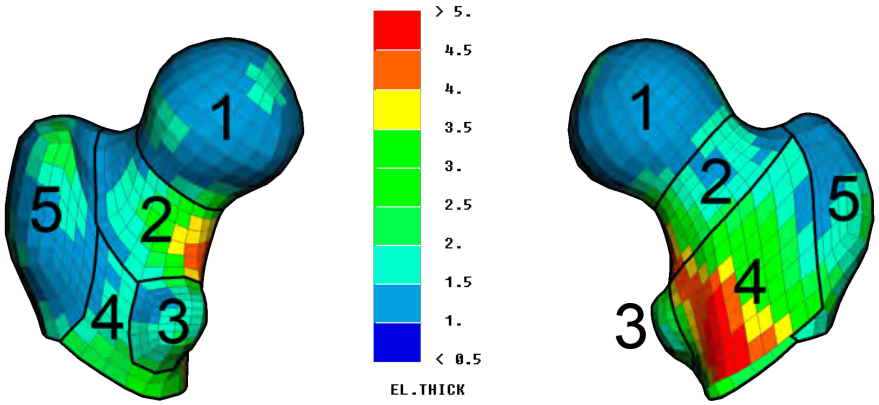

Fig. 4. Resulting average cortical thickness of the proximal femur.

TABLE III
AVERAGE CORTICAL THICKNESS IN THE PROXIMAL FEMUR BY REGION (REGIONS ACCORDING TO FIG. 4)

Region	*Average cortical thickness [mm]*
Head (1)	1.39
Neck (2)	2.16
Lesser Trochanter (3)	1.91
Intertrochanteric (4)	3.09
Greater Trochanter (5)	1.57

TABLE IV
SUMMARY OF YOUNG'S MODULI AND YIELD STRESSES IN COMPRESSION AND TENSION FOR THE CORTICAL FEMUR BONE CALCULATED USING EXPERIMENTAL DATA BY [18]

Loading	*E [GPa]*	σ_y *[GPa]*
Compression	16.479	0.11365
Tension	16.384	0.06426

C. Material Data

1) Cortical Bone

A summary of the implemented values for the Young's modulus E and yield stress σ_y can be found in Table IV. The cortical bone was set to a uniform density of 1.8 g/cm³ throughout the whole model [27], [48]. The resulting true stress and true strain curves for tension and compression, are provided in Fig. 5, in which the identified yield points have been marked as a black dots (0.05% strain offset). The grey line shows the Young's modulus in compression.

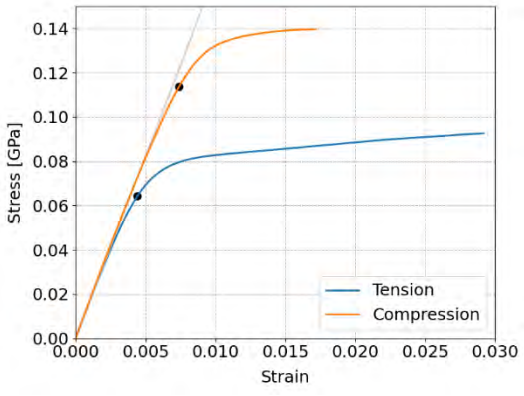

Fig. 5. Stress-strain curves for compression and tension for the cortical bone calculated using raw data from [18].

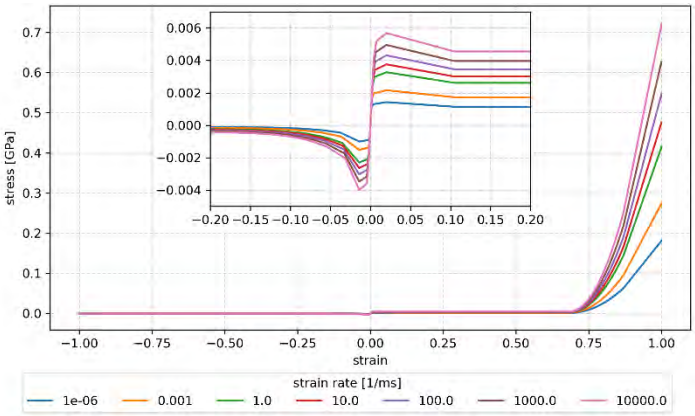

Fig. 6. Stress-strain curves for trabecular bone for different strain rates. Positive strain and stress are defined as compression in accordance with the material model *MAT83.

2) Trabecular Bone

The resulting strain-stress-curves are plotted in Fig. 6, which were implemented in *MAT83. Therefore, the material model's definitions for compression (positive strain/stress) and tension (negative stress/strain) were adopted. *MAT83 requires uniform endpoints for all implemented curves. In order to provide a detailed view, the smaller graph in the centre shows a detail of the curves, for the strain range of -0.2 to 0.2.

D. Validation

1) Sideways fall

The force-time histories predicted by the model (orange) have been compared to the respective curves from the experiments (black) from [28] in Fig. 7. The predicted force was evaluated via the contact force between the upper PMMA-pad and the greater trochanter. The simulated fracture forces are compared to the reported experimental fracture forces in Appendix D (Table D-I), where the respective strain values (PS99 and MPS) are given as well. A visual comparison of MPS of the SWF simulation compared to the reported strain distribution also derived by simulation by [28] showed comparable results. A plot of the MPS strain distribution in the cortical bone at time of fracture for specimen H1373R is shown in Appendix D (Fig. D-1). The definitions in parentheses next to the specimen numbering reflect abbreviations of the WHO classification for the degree of osteoporosis, *no* means normal (T-score > -1), *on* stands for osteopenic (-1 > T-score > -2.5) and *ot* for osteoporotic (T-score < -2.5). In addition, the age of the respective donor in years is shown in the heading of each diagram.

ISO scores revealed a higher rating for the experiments with specimens with normal bone density (mean R=0.82) as for osteopenic and osteoporotic specimens (mean R=0.56). Ratings R for all simulations are shown in Appendix D (Table D-I).

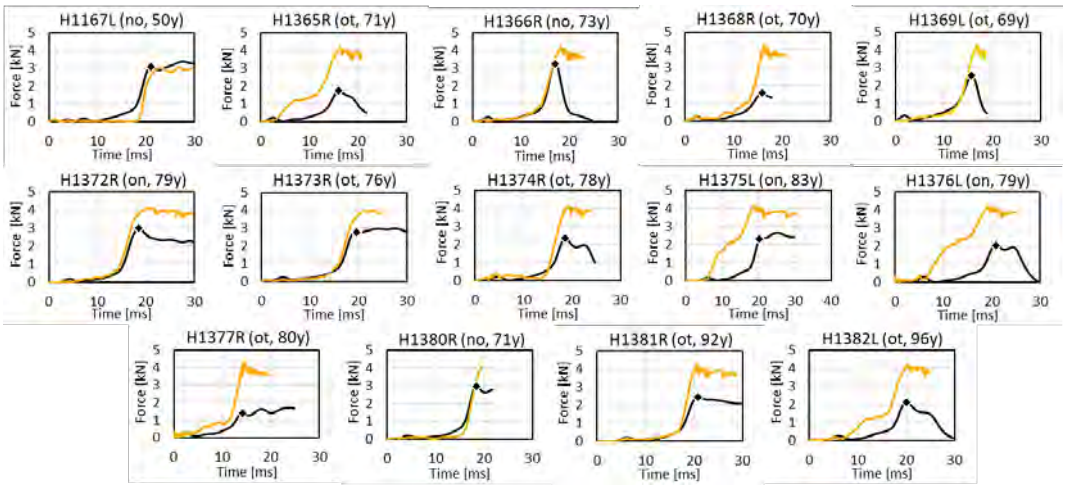

Fig. 7. Force curves from [28] (black) compared to the simulations of the SWF setup (orange).

2) Femur Shaft – Combined Loading and Three-point Bending

The simulation results (orange) and the experimental results (black) from [45] are compared in Fig. 8 for all 16 replicated tests by means of the impactor force over time. All test curves have been plotted until fracture occurred (marked with black rhomb). Time of fracture was determined as suggested by the authors of the experimental study [45]. Simulation results are shown for the full simulation time of 50 ms and 500 ms (in the simulations no fracture occurred as no failure was included in the applied material model). The heading of each diagram shows the test number and the abbreviations within parentheses summarises the respective loading condition (combined axial compression and bending (co) or bending (be)), the direction for the bending loading condition (posterior-anterior (PA) or anterior-posterior (AP)), side of which the femur was explanted (L-left, R-right), as well as the donor age in years. The dataset consisted largely of matching pairs of the left and right femur from the same donor, which can be observed as the same age is indicated for a left sided and right sided test.

It was observed that some simulations did not achieve the force level of the experimental curve as they reached a kind of force plateau at about 4 kN, caused by the start of yielding of the elastic-plastic bone material at this force magnitude. An oscillation about this plateau can be observed, caused by the dynamic loading speed in combination with the comparably small increase of impactor force after the start of material yielding. For test purposes, simulations were run exclusively with an elastic material, which did not show the force plateau, however they are not reported within this study. Detailed force and strain values for both the experiments by [45] and the simulations, are shown in Appendix D (Table D-II). MPS in the cortical bone was observed at the opposite side of impactor contact and are shown for Specimen 1.23 at time of strain evaluation in Appendix D (Fig. D-2).

An average ISO rating of R=0.78 was achieved with lowest rating *fair* for specimen 1.27 (R=0.70) and highest rating *good* for specimens 1.29 and 2.10 (R=0.88). ISO ratings for all specimens are included in Appendix D (Table D-II).

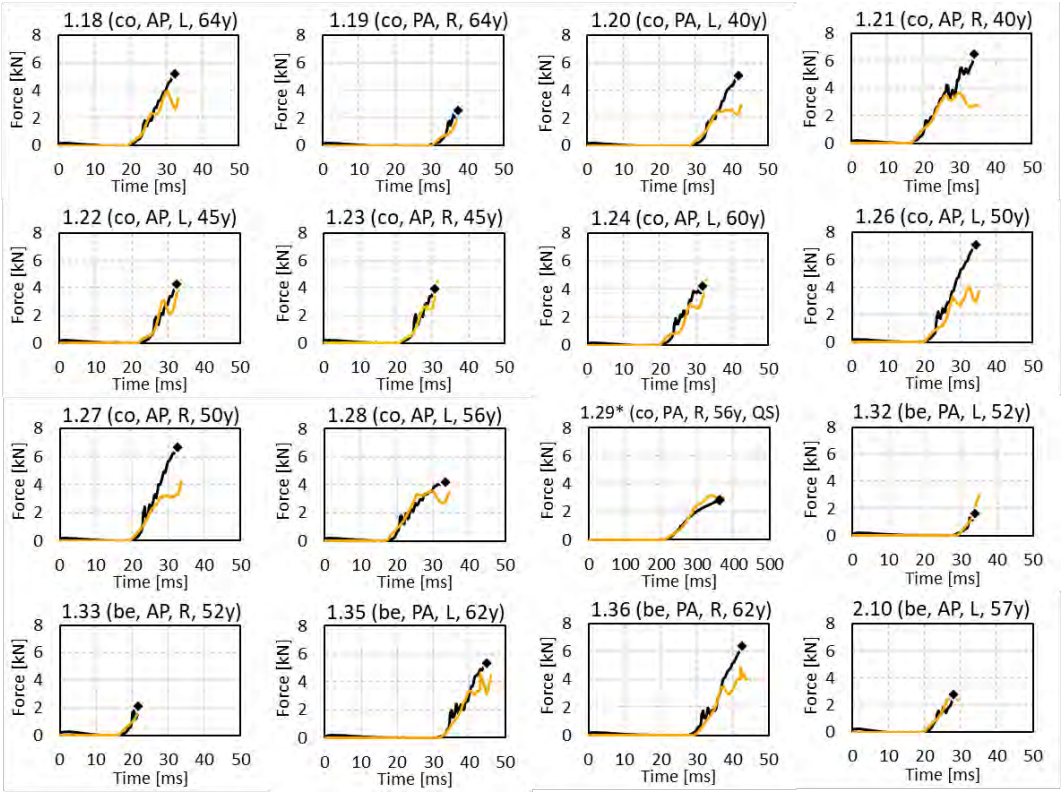

Fig. 8. Vertical impactor force over time from [45] (black) compared to our simulation of the femur shaft (orange). (PA=posterior-anterior, AP=anterior-posterior, co=combined loading, be=bending loading, QS=quasi static, R=right side, L=left side). Simulation 1.29 has been marked with an asterisk, as the experiment was run with a quasi-static impactor speed of 1 mm/s.

E. Injury Risk Curve

The derived parameters for the Weibull functions of the developed IRCs are summarised in Table V, while their 95% confidence intervals and the resulting curves for the 99th percentile principal strain (PS99) are plotted in Fig. 9. In addition to the PS99 strains at time of fracture, risk curves for the proximal femur and the femur shaft were also calculated using total MPS.

The IRC of the proximal femur was derived from simulations based on the sideways fall configuration experiments by [28], including the 11 simulations (excluding three tests with highest displacement at time of fracture) is shown in Fig. 9 (left). The corresponding curve for MPS values is shown in Appendix E (Fig, E-1, left).

On the right side of Fig. 9, the injury risk curve (PS99) for the femur shaft, based on 14 simulations replicating the tests by [45], is shown. Two simulations (lowest fracture force and therefore lowest impactor displacement at time of fracture in the experiments), suggesting comparatively small strain values in the simulations were excluded from the calculation of the IRC for the femur shaft. The corresponding curve, calculated using MPS is shown in Appendix E (Fig, E-1, right).

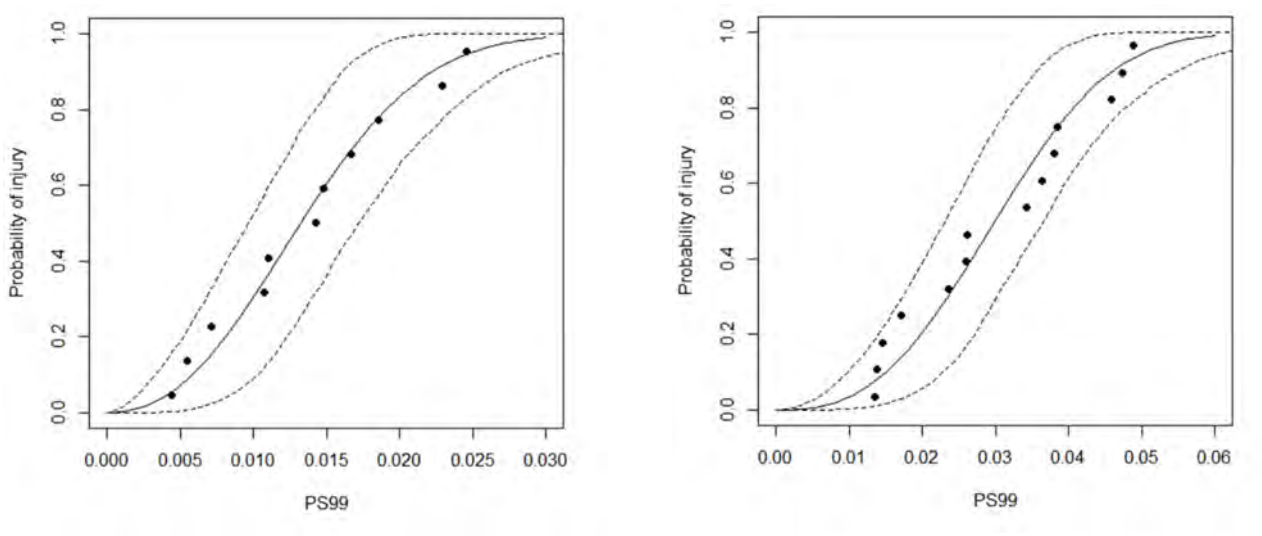

Fig. 9. Injury risk curve for the proximal femur (left) and the femur shaft (right), assuming a Weibull distribution with a 95% confidence interval using 99th percentile principal strains.

TABLE V
SUMMARY OF WEIBULL PARAMETERS FOR DERIVED INJURY RISK CURVES

		Shape factor (k)	Scale parameter (λ)	AIC	loglik
Proximal femur	MPS	2.6230	0.0245	-74.9	39.5
		[1.6353, 4.2072]	[0.0196, 0.0308]		
	PS99	2.2244	0.0149	-84.5	44.3
		[1.4187, 3.4877]	[0.0114, 0.0195]		
Femur shaft	MPS	2.7177	0.0302	-83.5	43.8
		[1.7686, 4.1763]	[0.0246, 0.0369]		
	PS99	2.7426	0.0342	-80.3	42.1
		[1.7878, 4.2072]	[0.0279, 0.0418]		

IV. DISCUSSION

A. Limitations

The aim of this study was to develop, calibrate and validate a femur model for a 50th percentile female HBM model at the age of 50, a stature of 162 cm and a weight of 62 kg. As available experimental measurements are limited in general with regard to age, several influences may be included that could bias the results, impacting the developed femur model, as well as the calculated IRCs.

Firstly, the mean age of the five individuals, whose cortical thickness of the proximal femur was averaged, was

close to 25 years instead the targeted 50 years. Furthermore, the identified material properties of the cortical bone may be influenced due to the average of the donors (mean age 76 years). However, it was decided to prioritise an averaged dataset instead of subject-specific material properties as this would have led to only one remaining sample for both datasets. Due to the fact that only one sample for the material data was younger than 50 [18] and only one sample for the geometry data was older than 50, it was not possible to develop a meaningful regression model. Therefore, age-dependent material behaviour has not been implemented in the model although several studies found a decreasing Young's modulus with increasing age [18], [49]–[51]. This decision was made as a wide range of Young's moduli derived from material tests of cortical bone have been reported in literature, as shown in Appendix B (Fig. B-1 and Table B-I). Secondly, increasing the Young modulus would not have improved the validation results.

The age in the SWF validation tests were also higher than the target age for the risk curve. Using the approach described in this paper where the displacement was prescribed on one generic femur, no significant correlation between the observed strain at the time of fracture and the subject age was observed, and therefore the age was not included in the risk curve.

The current material model does not take into account the anisotropic behaviour of the cortical bone [52]–[54]. In bending configurations this will be sufficient, although the model may not be sui-or torsional loadings or detailed fracture pattern analysis without further adjustments of the material model and validation [53].

Within the current study, the density of the trabecular bone was assumed to be constant, although it is known that is not the case [26], [55]–[56], as no dataset was available to be used as target. A sensitivity study was performed which is further explained in Section C.

Strain-rate dependency for the cortical bone was not modelled as results from material testing did not appear to have been finally conclusive [31][57]. The applied experimental data from [18] was only available for one strain rate ($2.5*10^{-4}\,s^{-1}$).

In the analysed accident data it was not possible to distinguish between injury sources. The proximal femur fractures could either have been sustained in the impact by the car or the ground.

B. Cortical Thickness

Although the sample for the definition of the average cortical thickness of the proximal femur contained data from a rather small sample of five individuals, the resulting averaged thicknesses by region are in line with other studies [58]–[61]. Other sources, such as [62], state slightly lower cortical thickness for individual regions of the proximal femur, however, this study was more focused on elderly people. During the meshing process of the proximal femur, slight deviation between the calculated average thickness and the final geometry of the solid elements were noted, especially in the region of the greater trochanter. Hence, it was decided to apply a mesh smoothing algorithm before the creation of the new trabecular solid elements. At single nodes, this caused deviations of the thickness up to 10%.

Different solid element formulations (*ELFORM*) for the cortical bone were tested using the validation setup for specimen H1366R from [28]. The default formulation EQ = 1 with default and adjusted hourglass model (HIQ = 5), fully integrated elements (EQ = 2) and fully integrated elements intended for solids with poor aspect ratio (EQ = -2), were compared. The observed differences in stiffness of the proximal femur were rather small. For ELFORM=1 and the default hourglass model, the hourglass energy was in the range of 10%. ELFORM EQ = -2 was chosen for the final model, as it showed a robust behaviour and a plausible strain pattern. Figures for force-time, total, internal, and hourglass energy for each element formulation, are supplied in Appendix F (Fig, F-1)).

C. Material Properties

The material properties for the cortical bone calculated on basis of experimental raw data from [18] are also in line with the literature. The Young's modulus of around 16 GPa corresponds to the mentioned density relationship by [26], assuming the density of cortical bone to be 1.8 g/cm³ [27], [63]. It is also consistent with material properties published in the literature. A Young's modulus of 16 GPa is highlighted by a blue vertical line in the boxplot summarising values from [20], [32], [64]–[72] as shown in Appendix B (Fig. B-1)).

Reference [18] showed no significant differences for the Young's modulus derived from tension and compression loading. The reported data showed a slightly lower, Young modulus for tension loading, which was in line with the calculation conducted in this study on the basis of the same experimental data. Hence, it was decided to implement separate values of the Young's modulus for tension and compression loading

Scaling of the cortical material in the proximal region was implemented in the simulation based on findings by [20], who found a 24% decrease in the elastic modulus measured in the femoral metaphysis compared to the shaft for test purposes, however the results (not reported) were considered to require further improvement. The samples used for the macro-mechanical testing by [18] were extracted from mid-shaft of the femur, indicating that the calculated properties must be scaled when applying them for the proximal femur. This assumption is also supported by implementation by [23]–[24], who scaled the shafts Young's modulus by 66% for the neck, 85% for the head [23], 25% for the metaphysis, and 66% for the epiphyses [24]. In the final model, a stiffness reduction of 66% for the femur neck and head was implemented based on the ratios from [24], who refers to [21]–[22] for the magnitude. This decision was also supported by the comparison of the simulation result with the experimental data using a specimen from a 50 year old female donor with normal bone density (H1167L in [28]), where force-time histories matched very nicely.

As the density of the trabecular bone was set to constant, although it is known that it is not the case, the influence of different densities for the trabecular bone were studied using one load-case from [28] as an example, that is shown in Appendix F (Fig, F-3). The defined density of 0.27 g/cm³ represents a mean value, but the real density of the trabecular bone in the proximal femur is not homogeneous and the material shows different behaviour depending on the anatomical site [26], [55]–[56]. The density was halved (0.12 g/cm³), doubled (0.56 g/cm³) and the trabecular bone was removed completely from the femur. An influence on the overall stiffness and the MPS values in the cortical bone was noted. In future studies, inhomogeneous densities, and corresponding property-relationships, would further improve the model. Therefore, data sources defining a generic average density distribution for the femoral head would be beneficial.

Failure was not considered in the material model. As it was aimed at deriving a probabilistic injury method, element erosion was avoided. Furthermore, the failure models, as implemented in LS-Dyna still have several limitations when it comes to modelling bone fractures [53].

D. Validation Results

As displacements, not forces, were prescribed to derive the strain-based risk curves, it has been assumed that it is not critical that maximum forces deferred in some of the replicated experiments.

The SWF simulations over predicted the experimental force in several cases. However, 12 out of 15 specimens used by [28] suffered from reduced bone mineral density, which was found to influence bone strength, fracture loads and the femoral stiffness, negatively [34][38][42][56]. Three specimens were found to be osteopenic and nine diagnosed as suffering from osteoporosis, which can be explained by donor age. Implementing scaled cortical bone properties for the GT, neck and head, were found to be necessary, and led to smaller deviations with specimens of normal bone density. The simulated mean fracture force down to 3.6 kN, is comparable to other experiments carried out with similar setups, where ultimate forces between 3-5 kN were reported [34][36][73]. Mean ISO ratings were higher for specimens with normal bone density (R=0.82) compared to specimen with reduced bone density (R=0.56). Finally, it is assumed that the proximal femur model shows a realistic behaviour regarding the SWF setup when compared to the specimens with normal bone density.

Simulations based on the combined axial compression and three-point bending as well as pure three point bending of the femoral shaft, showed only minor deviation to the experimental data from [45]. Mean age of the donors for the 16 femur shaft tests was 53 years. In some simulations the developed femur model under predicted the peak force as yielding prevented an increase of impactor force over approx. 4kN. Comparing the mid-shaft cross section properties revealed that most of the under predicted specimens had significantly higher geometric properties compared to the simulation model. The slope of the force-time curves is in line with the test data, and shows a plausible bending behaviour of the femur shaft under both sole bending and combined loading conditions. The mean fracture force of the selected female femur tests was 4.4 kN (SD 1.7 kN). Yielding of the model occurred approximately at a force level of 4 kN. However, the simulations could not predict fracture forces above this force level. The comparison of mid-shaft cross sectional properties revealed a plausible reason for the observed differences. While the cross sectional area of the developed femur model was approx. 300 mm^2 in the mid-shaft region, the mean value of the tested femurs was 336 mm^2 [45]. The moment of inertia of the femur mid-shaft was also identified as an important predictor for femur fracture moment during the experiments by [45] [73]–[75]. The cross sectional area of the developed femur had been adjusted at five locations along the shaft to meet the values reported by the regression model of [15], for the targeted HBM anthropometry. Experiments

1.26 and 1.27 were conducted with femurs derived from the same 50 year old donor where across sectional area of 430 mm^2 and 414 mm^2 for the left and right side, respectively, were reported. The combined axial compression bending tests are more representative for vehicle occupants than for VRUs. However, the experimental results suggested no major reduction of bending strength was caused by the axial preload. Hence, it was decided to include combined loaded specimens, in addition to the specimens loaded under sole bending, which have been assumed to be most relevant for VRU accidents. Both loading types led to midshaft fractures which were found to be very relevant for pedestrian and cyclists in the accident analysis.

E. Injury Risk Curve

The developed IRCs refer to experiments with femurs of female donors (also including one male) where injuries had occurred. The age of the tested specimen (mean age 76 years) for the proximal femur, may lead to an overestimated injury risk [76]. Implementation of an age-factor was tested within the survival analysis, however it did not lead to meaningful results. For the development of the proximal femur IRC three tests were excluded since the strains obtained were notably larger due to greater experimental displacement at time of fracture. For the calculation of the IRC for the femur shaft, two experiments with the lowest fracture force were excluded as this might lead to implausible results.

The chosen parameterised Weibull survival function has also been used previously to predict hip fractures [77]. However, the risk curve developed in that study is based on forces and therefore not directly applicable for HBM simulations. In our study, model-specific risk curves were derived.

F. Outlook

To facilitate availability of two comparable models, the applied methods will be repeated for the male. The femur model can be used within the full VIVA+ 50F HBM to study the injury risk in VRU accidents and to investigate the reasons for sex-specific differences, which have been observed when analysing real-world accidents. The femur and the derived risk curves will be further validated by comparison with full-scale post-mortem human subject (PMHS) tests and real-world accidents. Thanks to the open-source approach of the VIVA+ models, any researcher can further improve the model, add validation loadcases or refine the injury risk curve. The models and scripts used for preparing this manuscript is available on the VIRTUAL project OpenVT platform, https://virtual.openvt.eu/fem/viva, which is also where the final VIVA+ models will be available and contributor guidelines can be found.

V. CONCLUSIONS

A representative generic femur model of a 50^{th} percentile female was developed using available data for both, geometry, and material properties. The model was validated focusing on the proximal femur and femur shaft, since it was found that these areas are of particular interest for car-to-pedestrian and car-to-bicycle accidents. Model-specific injury risk curves based on the cortical principal strains were developed to predict proximal and femur shaft fractures. For the future, to further improve the validation work and make the injury risk curve more robust, it would be very valuable to have access to more data from female PMHSs, also covering a wider range of ages. The femur model can be used within the full VIVA+ 50F HBM to study the injury risk in VRU accidents and to investigate the reasons for sex-specific differences, which have been observed when analysing real-world accidents. To the best knowledge of the authors, no other openly available HBM including a specific injury risk curve for femur fractures is available.

VI. ACKNOWLEDGMENT

This study received funding from the European Union Horizon 2020 Research and Innovation Programme under Grant Agreement No. 768960. We would like to thank Mr. Özgür Cebeci from IATmbh (IAT Ingenieurgesellschaft fuer Automobiltechnik mbH, Berlin, Germany) for his valuable input and interesting discussions. Furthermore, we would like to thank Harris et al. from the University of Utah (Salt Lake City, Utah, USA) for generously sharing the CT images of femur heads and Uwe Wolfram from the Heriot-Watt University (Edinburgh, UK) for sharing the data of the cortical femur bone with us. The authors gratefully acknowledge the use of High-performance computing resources provided by the ZID (Zentraler Informatikdienst) at Graz University of Technology, (Graz, Austria) and thank BETA CAE Systems International AG (Root, Switzerland) for their support.

VII. REFERENCES

[1] World Health Organization. "2018. "Global status report on road safety 2018", *World Health Organization*, Geneva, Switzerland.

[2] Lanner D, Halldin P, Iraeus J, Holmqvist K, Mroz K, Pipkorn B *et al.* (2010) Evaluation of finite element human body models in lateral padded pendulum impacts to the shoulder. International Journal of Crashworthiness, **15**(2): pp.125–142.

[3] Park G, Kim T, Crandall JR, Svendsen A, Saunders N, Markusic C (2014) Evaluation of Biofidelity of Side Impact Computational Surrogates (ES-2re, WorldSID, GHBMC). *Proceedings of SAE 2014 World Congress & Exhibition,* 2014.

[4] Klug C, Feist F, Schneider B, Sinz W, Ellway J, van Ratingen M. (2019) Development Of A Certification Procedure For Numerical Pedestrian Models. The 26th International Technical Conference and exhibition on the Enhanced Safety of Vehicles (ESV).

[5] Leo C, Rizzi MC, Bos NM, Davidse RJ, Linder A, Tomasch E *et al.* (2021) Are There Any Significant Differences in Terms of Age and Sex in Pedestrian and Cyclist Accidents? Frontiers in Bioengineering and Biotechnology, **9**.

[6] Otte D, Jänsch M, Haasper C. (2012) Injury protection and accident causation parameters for vulnerable road users based on German In-Depth Accident Study GIDAS. Accident Analysis and Prevention, **44**(1): pp.149–153.

[7] Weijermars W, Bos N, Stipdonk HL. (2016) Serious road injuries in The Netherlands dissected. Traffic Injury Prevention, **17**(1): pp.73–79.

[8] Wisch M, Lerner M, Vukovic E, Hynd D, Fiorentino A, Fornells A. (2017) Injury Patterns of Older Car Occupants, Older Pedestrians or Cyclists in Road Traffic Crashes with Passenger Cars in Europe - Results from SENIORS. Proceedings of IRCOBI Conference, 2017, Antwerp, Belgium.

[9] Saadé J, Cuny S, Labrousse M, Song E, Chauvel C, Chrétien P. (2020) Pedestrian Injuries and Vehicles-related Risk Factors in Car-to-pedestrian Frontal Collisions. Proceedings of IRCOBI Conference, 2020, Munich, Germany.

[10] Larsson K-J, Pipkorn B, Iraeus J, Bolte JH, Agnew AM, Hu J *et al. (*2019) Evaluation of the Benefits of Parametric Human Body Model Morphing for Prediction of Injury to Elderly Occupants in Side Impact*. Proceedings of IRCOBI Conference,* 2019, Florence, Italy.

[11] Leo C, Klug C, Ohlin M, Linder A (2019) Analysis of pedestrian injuries in pedestrian-car collisions with focus on age and gender*. Proceedings of IRCOBI Conference,* 2019, Florence, Italy.

[12] Linder A, Davidse R, Iraeus J, John J, Schmitt K-U (2020) VIRTUAL - a European approach to foster the uptake of virtual testing in vehicle safety assessment*. Proceedings of Transport Research Arena TRA,* 2020, Helsinki.

[13] Schneider LW. "1983. "Development of anthropometrically based design specifications for an advanced adult anthropomorphic dummy family, volume 1. final report",

[14] eurostat. "Population on 1 January by age and sex", 2019.

[15] Klein KF, Hu J, Reed MP, Hoff CN, Rupp JD. (2015) Development and Validation of Statistical Models of Femur Geometry for Use with Parametric Finite Element Models. Annals of Biomedical Engineering, **43**(10): pp.2503–2514.

[16] Harris MD, Anderson AE, Henak CR, Ellis BJ, Peters CL, Weiss JA. (2011) Finite element prediction of cartilage contact stresses in normal human hips. Journal of Orthopaedic Research, **30**(7): pp.1133–1139.

[17] Väänänen SP, Jurvelin JS, Isaksson H. (2012) Estimation of 3D shape, internal density and mechanics of proximal femur by combining bone mineral density images with shape and density templates. Biomechanics and Modeling in Mechanobiology, **11**(6): pp.791–800.

[18] Mirzaali MJ, Schwiedrzik J, Thaiwichai S, Best JP, Michler J, Zysset PK *et al.* (2016) Mechanical properties of cortical bone and their relationships with age, gender, composition and microindentation properties in the elderly. Bone, **93**: pp.196–211.

[19] Koch D, Helbig M. "Introduction to Material Characterization", https://www.dynamore.de/de/download/presentation/2020/copy_of_dynamore-express-introduction-to-material-characterization [Accessed 26 April 2021].

[20] Lotz JC, Gerhart TN, Hayes WC. (1991) Mechanical properties of metaphyseal bone in the proximal femur. Journal of biomechanics, **24**(5): pp.317–329.
[21] Atkinson PJ. "A stress-based damage criterion to predict articular joint injury from subfracture insult: Michigan State University1998.
[22] Mente PL, Lewis JL. (1994) Elastic modulus of calcified cartilage is an order of magnitude less than that of subchondral bone. Journal of Orthopaedic Research, **12**(5): pp.637–647.
[23] Untaroiu CD, Yue N, Shin J. (2013) A finite element model of the lower limb for simulating automotive impacts. Annals of Biomedical Engineering, **41**(3): pp.513–526.
[24] Beillas P, Begeman PC, Yang KH, King AI, Arnoux PJ, Kang HS *et al.* (2001) Lower Limb: Advanced FE Model and New Experimental Data. Stapp Car Crash Journal, **45**: pp.469–494.
[25] Kelly N, McGarry JP. (2012) Experimental and numerical characterisation of the elasto-plastic properties of bovine trabecular bone and a trabecular bone analogue. Journal of the mechanical behavior of biomedical materials, **9**: pp.184–197.
[26] Morgan EF, Bayraktar HH, Keaveny TM. (2003) Trabecular bone modulus–density relationships depend on anatomic site. Journal of biomechanics, **36**(7): pp.897–904.
[27] Carter DR, Hayes WC. (1977) The compressive behavior of bone as a two-phase porous structure. The Journal of bone and joint surgery. American volume, **59**(7): pp.954–962.
[28] Ariza OR, Gilchrist SM, Widmer RP, Guy P, Ferguson SJ, Cripton PA *et al.* (2015) Comparison of explicit finite element and mechanical simulation of the proximal femur during dynamic drop-tower testing. Journal of biomechanics, **48**(2): pp.224–232.
[29] Enns-Bray WS, Bahaloo H, Fleps I, Ariza OR, Gilchrist SM, Widmer R *et al.* (2018) Material mapping strategy to improve the predicted response of the proximal femur to a sideways fall impact. Journal of the mechanical behavior of biomedical materials, **78**: pp.196–205.
[30] Helgason B, Gilchrist SM, Ariza OR, Chak JD, Zheng G, Widmer RP *et al.* (2014) Development of a balanced experimental-computational approach to understanding the mechanics of proximal femur fractures. Medical engineering & physics, **36**(6): pp.793–799.
[31] Hansen U, Zioupos P, Simpson R, Currey JD, Hynd D. (2008) The effect of strain rate on the mechanical properties of human cortical bone. Journal of biomechanical engineering, **130**(1): p.11011.
[32] Bayraktar HH, Morgan EF, Niebur GL, Morris GE, Wong EK, Keaveny TM. (2004) Comparison of the elastic and yield properties of human femoral trabecular and cortical bone tissue. Journal of biomechanics, **37**(1): pp.27–35.
[33] Backman S. (1957) The proximal end of the femur: investigations with special reference to the etiology of femoral neck fractures; anatomical studies; roentgen projections; theoretical stress calculations; experimental production of fractures. Acta radiologica. Supplementum(146): pp.1–166.
[34] Courtney AC, Wachtel EF, Myers ER, Hayes WC. (1994) Effects of loading rate on strength of the proximal femur. Calcified Tissue International, **55**(1): pp.53–58.
[35] Lochmüller E-M, Groll O, Kuhn V, Eckstein F. (2002) Mechanical strength of the proximal femur as predicted from geometric and densitometric bone properties at the lower limb versus the distal radius. Bone, **30**(1): pp.207–216.
[36] Boehm HF, Horng A, Notohamiprodjo M, Eckstein F, Burklein D, Panteleon A *et al.* (2008) Prediction of the fracture load of whole proximal femur specimens by topological analysis of the mineral distribution in DXA-scan images. Bone, **43**(5): pp.826–831.
[37] de Bakker PM, Manske SL, Ebacher V, Oxland TR, Cripton PA, Guy P. (2009) During sideways falls proximal femur fractures initiate in the superolateral cortex: evidence from high-speed video of simulated fractures. Journal of biomechanics, **42**(12): pp.1917–1925.
[38] Eckstein F, Wunderer C, Boehm HF, Kuhn V, Priemel M, Link TM *et al.* (2004) Reproducibility and side differences of mechanical tests for determining the structural strength of the proximal femur. Journal of Bone and Mineral Research, **19**(3): pp.379–385.
[39] Jazinizadeh F, Mohammadi H, Quenneville CE. (2020) Comparing the fracture limits of the proximal femur under impact and quasi-static conditions in simulation of a sideways fall. Journal of the mechanical behavior of biomedical materials, **103**.
[40] Le Corroller T, Halgrin J, Pithioux M, Guenoun D, Chabrand P, Champsaur P. (2012) Combination of texture

analysis and bone mineral density improves the prediction of fracture load in human femurs. Osteoporosis International, **23**(1): pp.163–169.

[41] Nishiyama KK, Gilchrist SM, Guy P, Cripton PA, Boyd SK. (2013) Proximal femur bone strength estimated by a computationally fast finite element analysis in a sideways fall configuration. Journal of biomechanics, **46**(7): pp.1231–1236.

[42] Ariza OR. "A novel approach to finite element analysis of hip fractures due to sideways falls, Vancouver: University of British Columbia2014.

[43] Gilchrist SM, Guy P, Cripton PA. (2013) Development of an inertia-driven model of sideways fall for detailed study of femur fracture mechanics. Journal of biomechanical engineering, **135**(12): p.121001.

[44] Gilchrist SM, Nishiyama KK, de Bakker PM, Guy P, Boyd SK, Oxland TR *et al.* (2014) Proximal femur elastic behaviour is the same in impact and constant displacement rate fall simulation. Journal of biomechanics, **47**(15): pp.3744–3749.

[45] Ivarsson BJ, Genovese D, Crandall JR, Bolton JR, Untaroiu CD, Bose D. (2009) The tolerance of the femoral shaft in combined axial compression and bending loading. Stapp Car Crash Journal, **53**: pp.251–290.

[46] Vehicle Safety Institute - Graz University of Technology. "2021. "Dynasaur",

[47] Peres J, Auer S, Praxl N (2016) Development and comparison of different injury risk functions predicting pelvic fractures in side impact for a Human Body Model*. Proceedings of IRCOBI Conference,* 2016, Seoul, South Korea.

[48] Gibson LJ. (1985) The mechanical behaviour of cancellous bone. Journal of biomechanics, **18**(5): pp.317–328.

[49] Mosekilde L, Mosekilde L, Danielsen CC. (1987) Biomechanical competence of vertebral trabecular bone in relation to ash density and age in normal individuals. Bone, **8**(2): pp.79–85.

[50] Wang X, Shen X, Li X, Mauli Agrawal C. (2002) Age-related changes in the collagen network and toughness of bone. Bone, **31**(1): pp.1–7.

[51] Dokko Y, Ito O, Ohashi K (2009) Development of Human Lower Limb and Pelvis FE Models for Adult and the Elderly*. Proceedings of SAE World Congress & Exhibition,* 2009.

[52] Morgan EF, Unnikrisnan GU, Hussein AI. (2018) Bone Mechanical Properties in Healthy and Diseased States. Annual review of biomedical engineering, **20**: pp.119–143.

[53] Khor F, Cronin DS, Watson B, Gierczycka D, Malcolm S. (2018) Importance of asymmetry and anisotropy in predicting cortical bone response and fracture using human body model femur in three-point bending and axial rotation. Journal of the mechanical behavior of biomedical materials, **87**: pp.213–229.

[54] Shahar R, Zaslansky P, Barak M, Friesem AA, Currey JD, Weiner S. (2007) Anisotropic Poisson's ratio and compression modulus of cortical bone determined by speckle interferometry. Journal of biomechanics, **40**(2): pp.252–264.

[55] Bauer JS, Kohlmann S, Eckstein F, Mueller D, Lochmüller E-M, Link TM. (2006) Structural Analysis of Trabecular Bone of the Proximal Femur Using Multislice Computed Tomography: A Comparison with Dual X-Ray Absorptiometry for Predicting Biomechanical Strength In Vitro. Calcified Tissue International, **78**(2): pp.78–89.

[56] Eckstein F, Lochmüller E-M, Lill CA, Kuhn V, Schneider E, Delling G *et al.* (2002) Bone strength at clinically relevant sites displays substantial heterogeneity and is best predicted from site-specific bone densitometry. Journal of Bone and Mineral Research, **17**(1): pp.162–171.

[57] McElhaney JH. (1966) Dynamic response of bone and muscle tissue. Journal of applied physiology, **21**(4): pp.1231–1236.

[58] Ramme AJ, Vira S, Hotca A, Miller R, Welbeck A, Honig S *et al.* (2019) A Novel MRI Tool for Evaluating Cortical Bone Thickness of the Proximal Femur. Bulletin of the Hospital for Joint Disease (2013), **77**(2): pp.115–121.

[59] Treece G, Poole KES, Gee A. (2012) Imaging the femoral cortex: thickness, density and mass from clinical CT. Medical image analysis, **16**(5): pp.952–965.

[60] Du W, Zhang J, Hu J (2018) A Method to Determine Cortical Bone Thickness of Human Femur and Tibia Using Clinical CT Scans*. Proceedings of IRCOBI Conference,* 2018, Athens, Greece.

[61] Snedeker JG, Walz FH, Muser MH. (2003) Assessment of pelvis and upper leg injury risk in car-pedestrian collisions: Comparison of accident statistics, impactor tests and a human body finite element model. Stapp

Car Crash Journal(47): pp.437–457.
[62] Yang L, Burton AC, Bradburn M, Nielson CM, Orwoll ES, Eastell R. (2012) Distribution of bone density in the proximal femur and its association with hip fracture risk in older men: the MrOS Study. Journal of Bone and Mineral Research, **27**(11): pp.2314–2324.
[63] Helgason B, Gilchrist SM, Ariza OR, Vogt PJ, Enns-Bray WS, Widmer RP *et al.* (2016) The influence of the modulus-density relationship and the material mapping method on the simulated mechanical response of the proximal femur in side-ways fall loading configuration. Medical engineering & physics, **38**(7): pp.679–689.
[64] Evans FG, Lebow M. (1951) Regional differences in some of the physical properties of the human femur. Journal of applied physiology, **3**(9): pp.563–572.
[65] Sedlin ED, Hirsch C. (1966) Factors affecting the determination of the physical properties of femoral cortical bone. Acta Orthopaedica Scandinavica, **37**(1): pp.29–48.
[66] Mather BS. (1968) Variation with age and sex in strength of the femur. Medical and biological engineering, **6**(2): pp.129–132.
[67] Yamada H. "1970. "Strength of biological materials", *The Williams & Wilkins Company*, Baltimore.
[68] Saha S, Hayes WC. (1976) Tensile impact properties of human compact bone. Journal of biomechanics, **9**(4): pp.243–251.
[69] Fung Y-C. "1993. "Biomechanics: Mechanical Properties of Living Tissues", *Springer New York*, New York, NY.
[70] Keller TS, Mao Z, Spengler DM. (1990) Young's modulus, bending strength, and tissue physical properties of human compact bone. Journal of Orthopaedic Research, **8**(4): pp.592–603.
[71] Currey JD. (2004) Tensile yield in compact bone is determined by strain, post-yield behaviour by mineral content. Journal of biomechanics, **37**(4): pp.549–556.
[72] Cuppone M, Seedhom BB, Berry E, Ostell AE. (2004) The Longitudinal Young's Modulus of Cortical Bone in the Midshaft of Human Femur and its Correlation with CT Scanning Data. Calcified Tissue International, **74**(3): pp.302–309.
[73] Forman JL, del Pozo de Dios, Eduardo, Symeonidis I, Duart J, Kerrigan JR, Salzar RS *et al. (*2012) Fracture Tolerance Related to Skeletal Development and Aging Throughout Life: 3-Point Bending of Human Femurs*. Proceedings of IRCOBI Conference,* 2012, Dublin, Ireland.
[74] Funk JR, Kerrigan JR, Crandall JR. (2004) Dynamic bending tolerance and elastic-plastic material properties of the human femur. Annual Proceedings / Association for the Advancement of Automotive Medicine, **48**: pp.215–233.
[75] Kennedy EA, Hurst WJ, Stitzel JD, Cormier JM, Hansen GA, Smith EP *et al.* (2004) Lateral and posterior dynamic bending of the mid-shaft femur: fracture risk curves for the adult population. Stapp Car Crash Journal, **48**: pp.27–51.
[76] Praxl N. (2011) How reliable are injury risk curves? 22nd International Technical Conference on the Enhanced Safety of Vehicles (ESV).
[77] Kleiven S. (2020) Hip fracture risk functions for elderly men and women in sideways falls. Journal of biomechanics, **105**: p.109771.
[78] Mather BS. (1967) The symmetry of the mechanical properties of the human femur. Journal of Surgical Research, **7**(5): pp.222–225.
[79] Reilly DT, Burstein AH, Frankel VH. (1974) The elastic modulus for bone. Journal of biomechanics, **7**(3): pp.271–275.
[80] Reilly DT, Burstein AH. (1975) The elastic and ultimate properties of compact bone tissue. Journal of biomechanics, **8**(6): pp.393–405.
[81] Burstein AH, Reilly DT, Martens M. (1976) Aging of bone tissue: mechanical properties. The Journal of bone and joint surgery. American volume, **58**(1): pp.82–86.
[82] Currey JD, Foreman J, Laketić I, Mitchell J, Pegg DE, Reilly GC. (1997) Effects of ionizing radiation on the mechanical properties of human bone. Journal of Orthopaedic Research, **15**(1): pp.111–117.

APPENDIX A

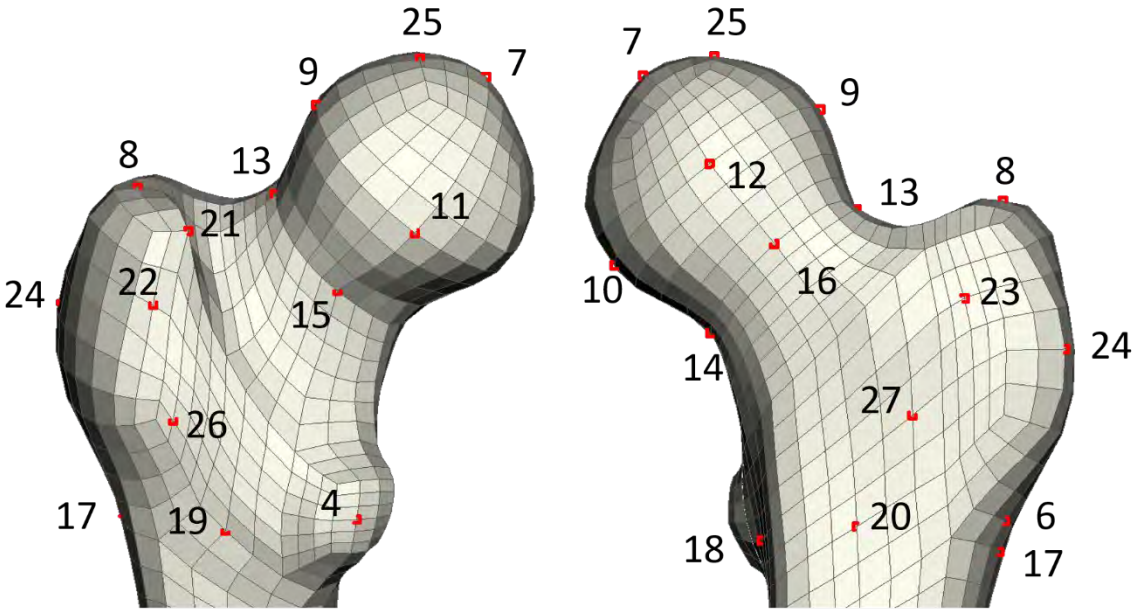

Fig. A-1. Landmarks used to morph cortical thickness specimen to target geometry of the proximal femur. Since the supplied samples were cut at varying heights of their distal end, Landmarks 17-20 were moved up to the same level as Landmark 4. Internal Landmarks 1, 2, 3 and 5 were not used and are therefore not shown.

APPENDIX B

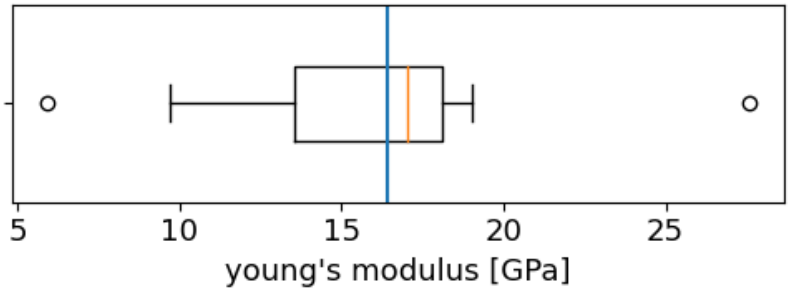

Fig. B-1. Boxplot of selected literature data of the Young's modulus derived from human femur material tests (references marked with § in Table B-I). The Young's modulus of 16.4 GPa (rounded value of the implemented elastic modulus) was marked with the vertical blue line.

TABLE B-I
COMPARISON OF YOUNG'S MODULI FOR THE CORTICAL BONE OF THE FEMUR FOUND IN LITERATURE
(* INCLUDES SAMPLES FROM TIBIA, § INCLUDED IN FIG. B-1)

Source	Specimen type	Specimen location	Young's modulus [GPa]
[64]§	Flat – Tensile (wet)	Femur (shaft)	15.7
[65]§	Flat – Tensile (wet)	Femur (shaft)	4.4-7.2
[65]	Flat – Bending (wet)	Femur (shaft)	10.4-19.3
[57]§	Rectangular – Compression	Femur (shaft)	15.2-42.1
[78]	Bending	Femur	7.6-19.0
[66]§	Bending	Femur	13.2
[67]§	(wet)	Femur	17.3
[79]	Rectangular – Tensile (wet)	Femur (shaft)	11.4-19.3
[79]	Rectangular – Compression (wet)	Femur (shaft)	15.1-19.7
[80]	Round – Tensile (wet)	Femur (shaft)	15.6-17.9
*[81]**	Rectangular – Tensile (wet)	Femur (shaft)	15.6-17.7
[68]§	Flat – Tensile	Femur (shaft)	14.5
[69]§	Tensile	Femur	17.6
[70]§	Rectangular – Bending	Femur (shaft)	12.1
[20]§	Rectangular – Bending	Femur (neck)	9.7
[82]	Rectangular – Bending	Femur (shaft)	9.1-13.6
[71]§	Square - Tension	Femur	16.7
[72]§	Flat – Bending	Femur (shaft)	18.6
[32]§	Rectangular – Tension (wet)	Femur (shaft)	17.8
[18]§	Dumbbell (wet) - Tension	Femur (shaft)	18.2
[18]§	Dumbbell (wet) - Compression	Femur (shaft)	19.0

APPENDIX C

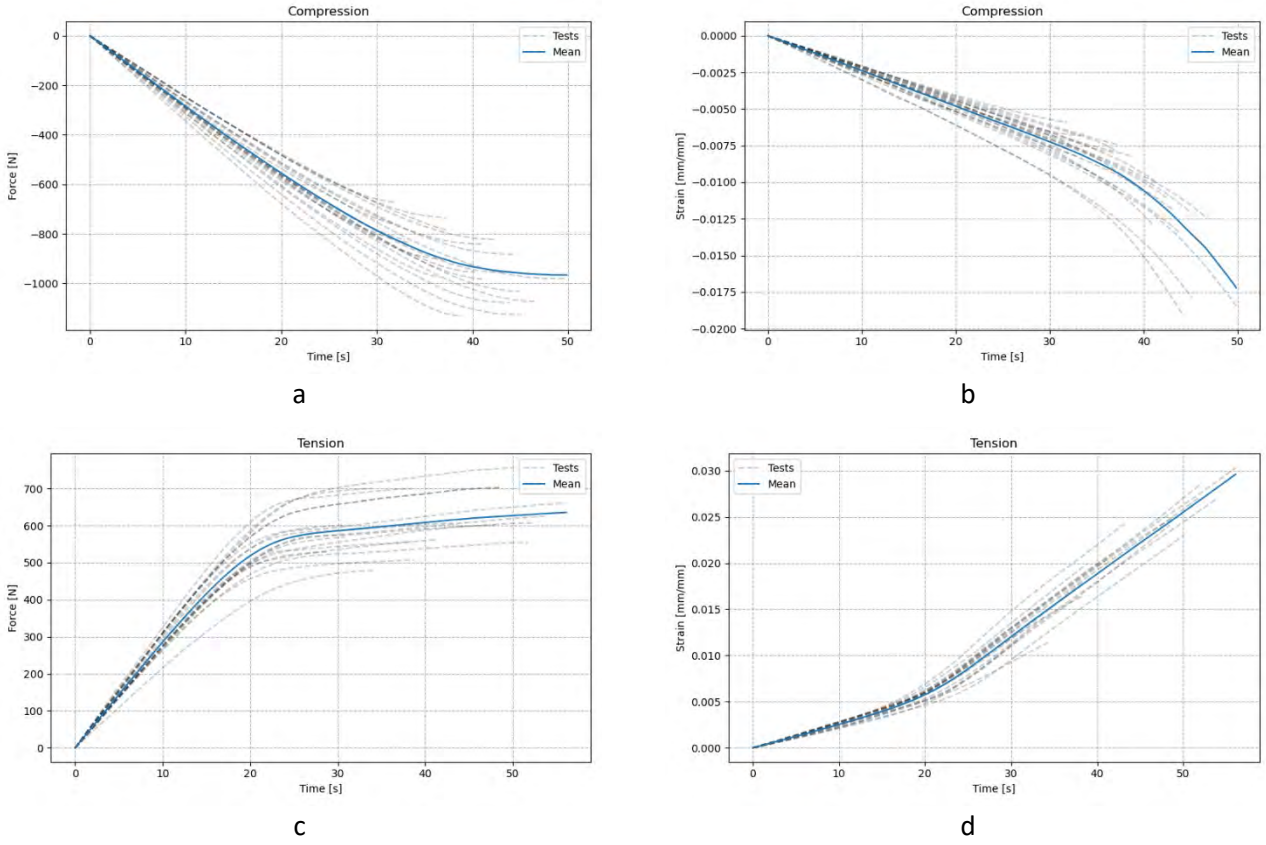

Fig. C-1. Calculated mean curves based on material testing data supplied by [18] of human femoral cortical bone: a = force-time in compression, b = strain-time in compression, c = force-time in tension, d = strain over time in tension.

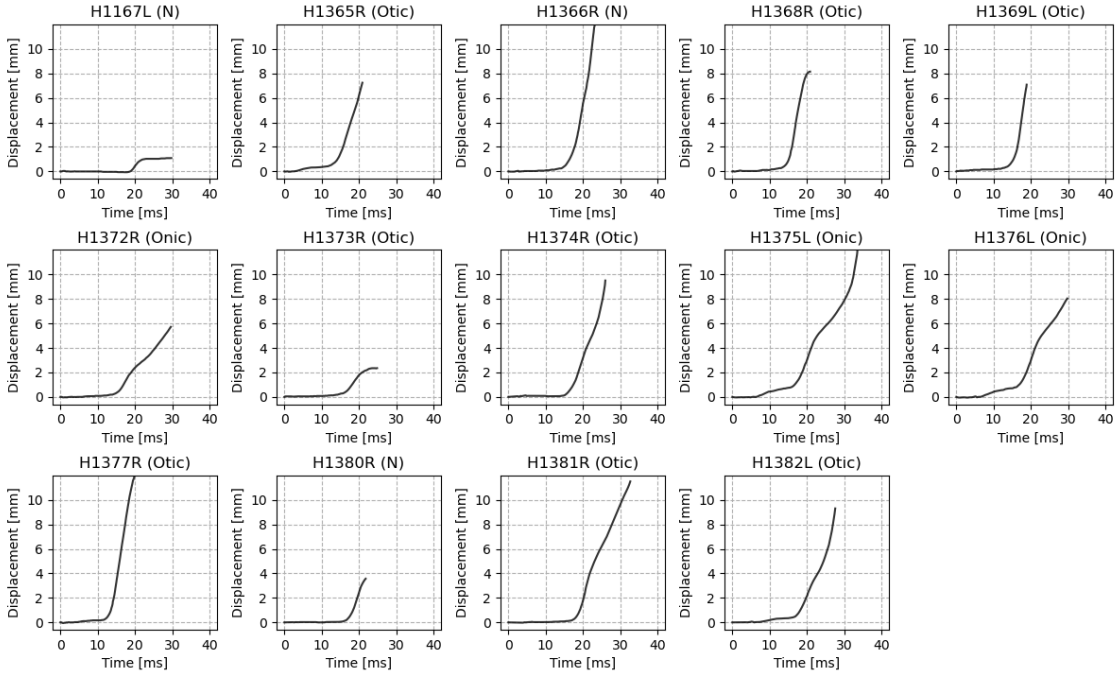

Fig. C-2. Displacements of the contact interface between the upper potting and the greater trochanter from [25].

APPENDIX D

TABLE D-I
PROXIMAL FEMUR SIMULATIONS: FRACTURE FORCE FROM EXPERIMENT [28] AND SIMULATION, PS99 AND MPS STRAIN AT TIME OF FRACTURE (t_F) AND ISO RATING FOR VIVA+ FEMUR (SIMULATIONS MARKED WITH AN ASTERISK WERE EXCLUDED FROM INJURY RISK CURVE CALCULATION)

Specimen	Experimental fracture force [kN]	Simulated Force at t_F [kN]	Experimental displacement at t_F [mm]	PS99 at t_F [-]	MPS at t_F [-]	ISO ratings
H1167L	3.1	2.6	0.8	0.0044	0.0066	0.72
H1168R	3.7	3.4	1.2	0.0074	0.0133	0.36
H1365R	1.7	4.1	2.2	0.0246	0.0359	0.93
H1366R	3.2	3.5	1.4	0.0110	0.0203	0.42
H1368R	1.5	4.0	1.8	0.0167	0.0280	0.85
H1369L	2.6	3.5	1.2	0.0075	0.0140	0.87
H1372R	3.0	3.8	1.7	0.0148	0.0260	0.86
H1373R	2.8	3.7	1.5	0.0107	0.0204	0.70
H1374R	2.4	3.9	1.9	0.0185	0.0295	0.20
*H1375L**	2.3	4.0	4.0	0.0652	0.1120	0.33
*H1376L**	2.0	3.9	3.7	0.0576	0.1007	0.36
H1377R	1.4	3.8	1.8	0.0163	0.0295	0.82
H1380R	3.0	3.3	1.0	0.0058	0.0096	0.74
*H1381R**	2.4	3.7	2.9	0.0368	0.0610	0.46
H1382L	2.1	4.0	2.2	0.0229	0.0333	0.72

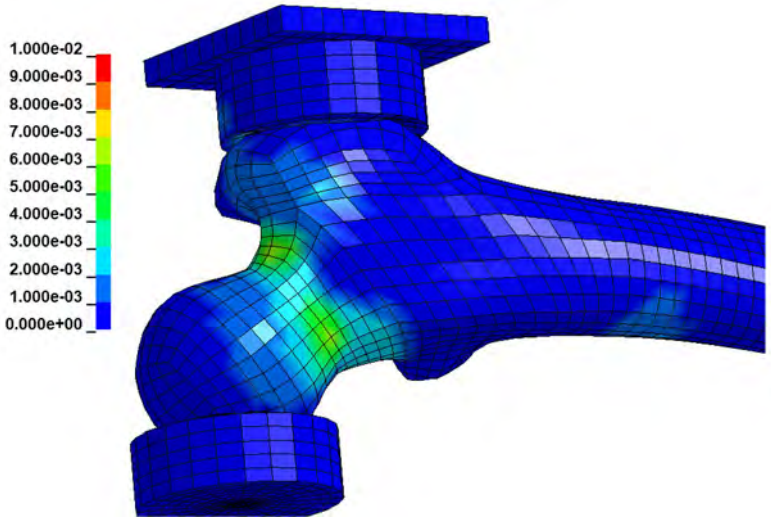

Fig. D-1. Maximum principal strain pattern of a proximal femur simulation (H1373R) at time of fracture (19.6 ms) as derived from the experiments by [28].

TABLE D-II
FEMUR SHAFT SIMULATIONS: FRACTURE FORCE FROM EXPERIMENT [45] AND SIMULATION, PS99 AND MPS STRAIN AT TIME OF FRACTURE AND ISO RATING FOR VIVA+ FEMUR (SIMULATIONS MARKED WITH AN ASTERISK WERE EXCLUDED FROM INJURY RISK CURVE CALCULATION)

Specimen	Experimental fracture force [kN]	Simulated Force at t_F [kN]	PS99 at t_F [-]	MPS at t_F [-]	ISO ratings
1.18	5.2	2.9	0.0237	0.0262	0.83
1.19	2.6	2.0	0.0143	0.0172	0.71
1.20	5.1	2.3	0.0345	0.0380	0.76
1.21	6.5	2.1	0.0428	0.0489	0.72
1.22	4.3	3.6	0.0205	0.0236	0.75
1.23	4.0	3.4	0.0121	0.0137	0.84
1.24	4.2	2.8	0.0118	0.0134	0.80
1.26	7.1	3.2	0.0234	0.0259	0.73
1.27	6.7	3.3	0.0320	0.0363	0.70
1.28	4.2	2.4	0.0414	0.0473	0.79
1.29	2.8	3.0	0.0287	0.0342	0.88
*1.32**	1.6	1.5	0.0056	0.0067	0.71
*1.33**	2.1	1.7	0.0050	0.0054	0.73
1.35	5.3	3.8	0.0350	0.0384	0.84
1.36	6.4	4.1	0.0409	0.0459	0.82
2.10	2.8	3.2	0.0128	0.0145	0.88

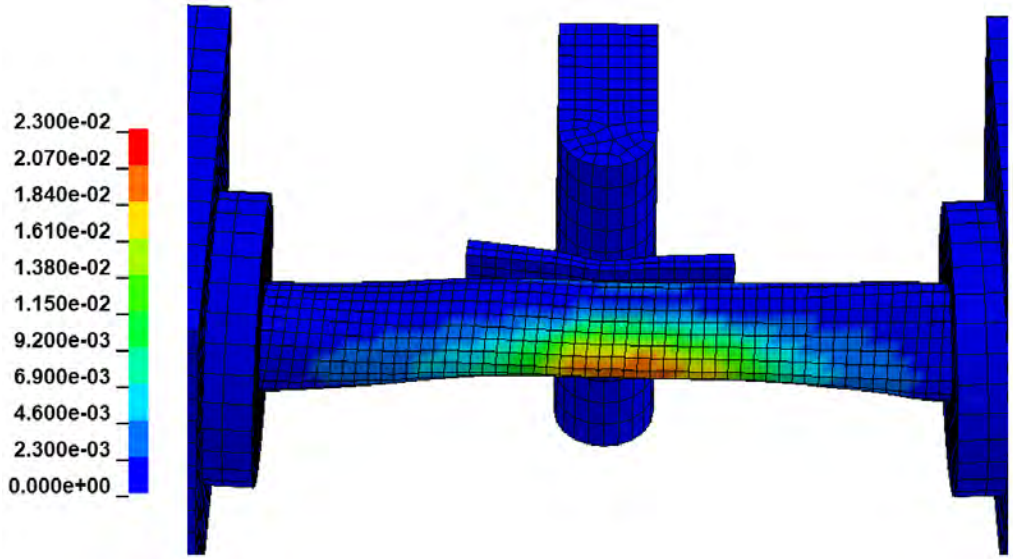

Fig. D-2. Maximum principal strain pattern of a femur shaft simulation (1.23) at time of fracture (30.6 ms) as derived from the experiments by [45].

APPENDIX E

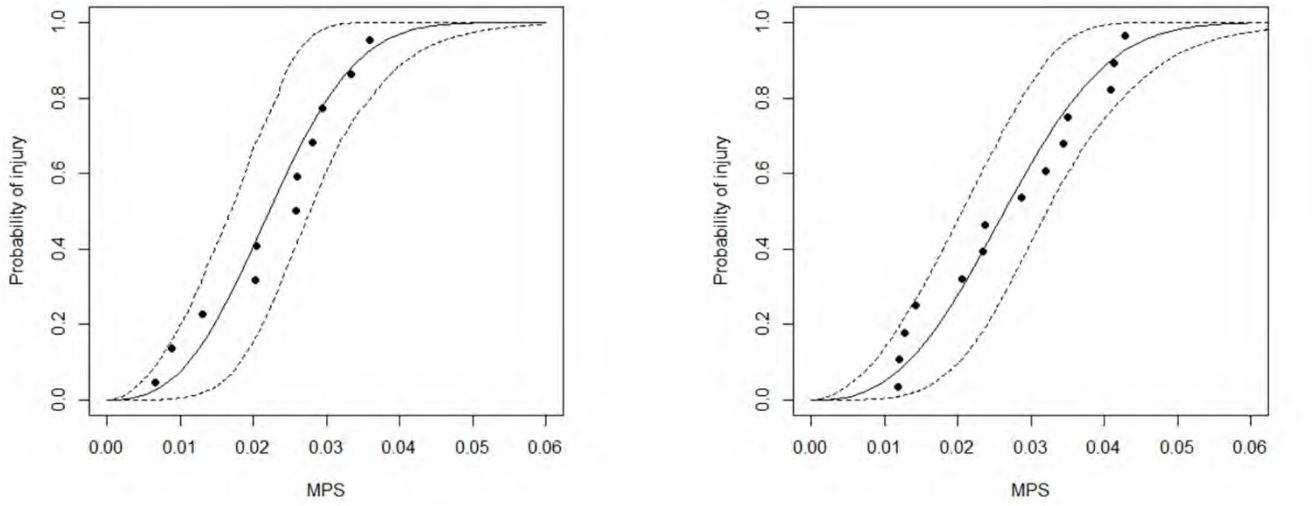

Fig. E-1. Injury risk curve of the proximal femur (left) and the femur shaft (right) obtained using maximum principal strain (MPS) in the cortical bone.

APPENDIX F

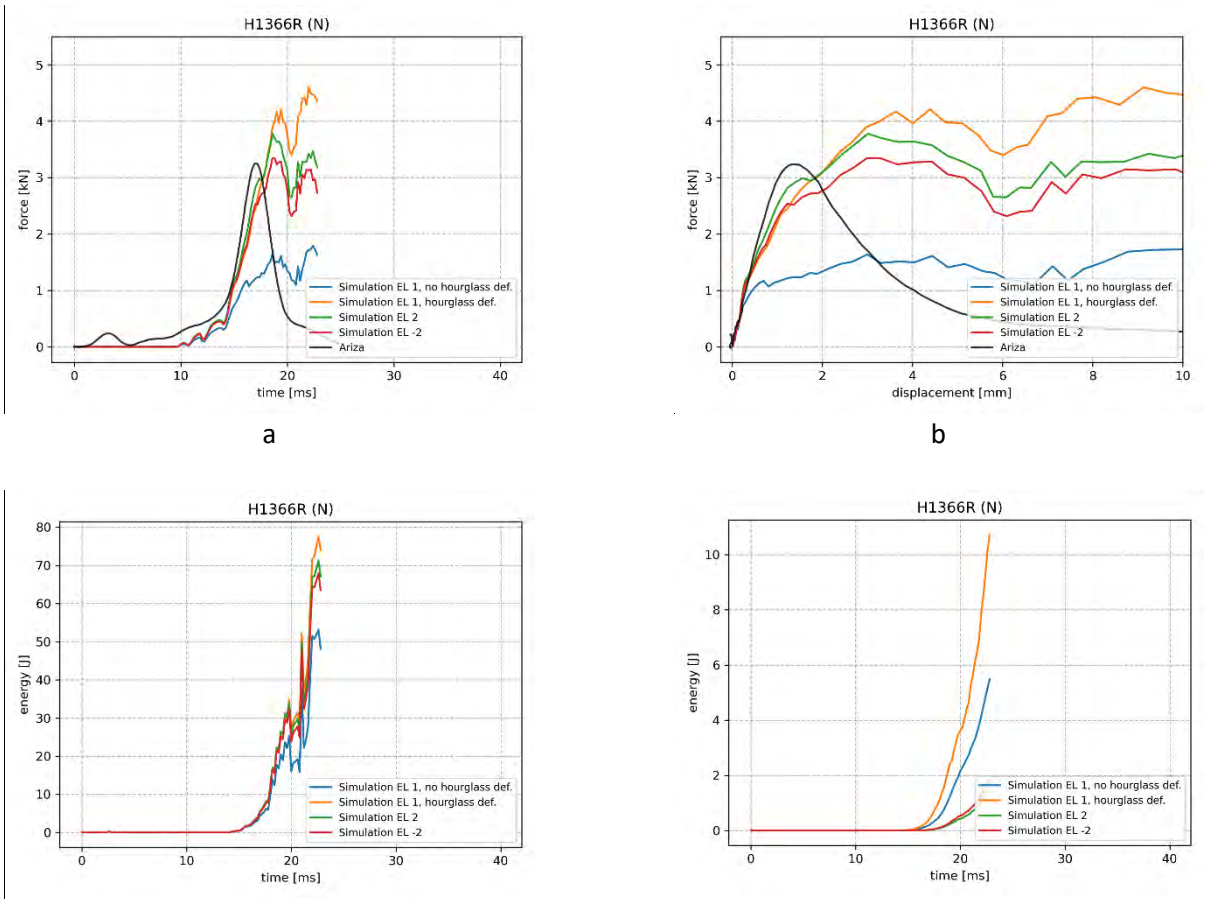

Fig. F-1. Influence of element formulation of the cortical bone elements in the proximal femur region included in the SWF simulation on force (a), force-displacement (b), total (c) and hourglass energy (d) for specimen H1366R from [28].

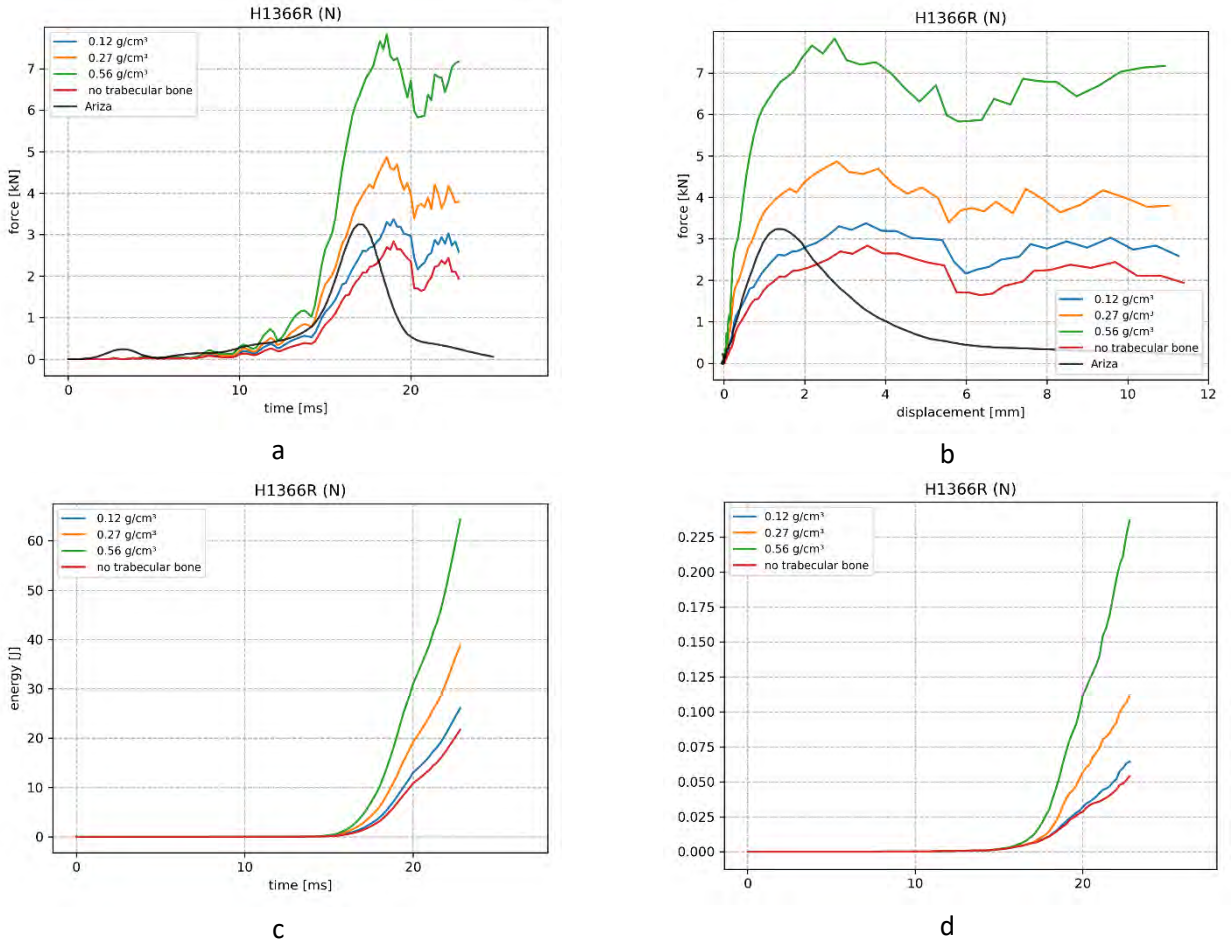

Fig. F-3. Influence of trabecular bone density in the proximal femur region included in the SFW simulation on force-time (a), force-displacement (b), internal energy (c), and cortical PS99 (d) for specimen H1366 from [28].